

Numerical Homogenization of Trabecular Bone Specimens using Composite Finite Elements

Martin Rumpf* Lars Ole Schwen* Hans-Joachim Wilke[†]
Uwe Wolfram[†]

Numerical homogenization is a tool to determine effective macroscopic material properties for microstructured materials. This tool is tailored and applied to ensembles of young and elder human and of porcine and bovine vertebral bone specimens. On the microscale of the spongiosa a linearized Lamé–Navier type elasticity model is assumed and the computed macroscopic material properties are represented by a general elasticity tensor. The computation is based on a suitable set of microscopic simulations on the cubic specimens for macroscopic strain scenarios. The subsequent evaluation of the effective stresses is used to determine effective linear elasticity tensors. A Composite Finite Element discretization is taken into account to resolve the complicated domain. The classical strain–stress and a corresponding variational homogenization approach are compared. In case of an (artificial) periodic microstructure, a fundamental cell is easily identified and a macroscopic unit strain can be imposed using affine-periodic boundary conditions. In contrast, statistically periodic structures require the identification of statistically representative prototype cells. Unit macroscopic strains are then imposed only in an approximate sense using displacement boundary conditions. The impact of the resulting boundary artifacts on the solution are compensated for via restricting the evaluation of effective stress to a suitably selected smaller subset of the cubic specimen. Furthermore, an optimization approach is used to identify possible axes of orthotropy of the resulting linear elasticity tensor. Finally, the different specimens of human, porcine and bovine spongiosa are analyzed statistically.

Keywords: Numerical Homogenization, Linearized Elasticity, Composite Finite Elements

AMS Subject Classifications (MSC2000): 65N30, 74B05, 74Q05, 74S05

1 INTRODUCTION

This article presents a numerical homogenization approach to non-periodic, microstructured elastic materials and applies it to different specimens of trabecular bone. The numerical method is based on a Composite Finite Elements discretization on the microscale of statistically representative fundamental cells.

*Institute for Numerical Simulation, University of Bonn, {martin.rumpf, ole.schwen}@ins.uni-bonn.de

[†]Institute of Orthopaedic Research and Biomechanics, Ulm University,
{hans-joachim.wilke, uwe.wolfram}@uni-ulm.de

Trabecular bone is the material microstructure of bones, which is of enormous biomechanical interest [1] and mainly located inside vertebral bodies and the epiphyses of long bones. It is often affected by osteoporosis [2, 3, 4] in elderly humans. Increasing costs (3.79 million osteoporotic fractures in Europe in 2000 lead to direct costs of 31.7 billion Euros [5], an estimate [6] for 2050 is 76.7 billion Euros) triggered the development of treatment techniques such as fixation devices [7], interbody fusion cages [8, 9], vertebroplasty and kyphoplasty [10, 11, 12], and special implant types [13, 14].

Finite element simulations for bone microstructure [15, 16, 17] are used to study the mechanical properties and assess those treatment techniques. Single-scale simulations resolving the trabecular microstructure, however, require huge amounts of computational resources [18]. Coarse scale continuum models rely on a proper identification of effective material properties which are very difficult to determine experimentally as the in situ loading conditions can hardly be reproduced [19]. In fact, instead of experimental measurements, finite element models can be used to determine these effective coarse scale material properties [20].

For macroscopically homogeneous microstructured materials, the terms numerical homogenization [21] or upscaling [22] denote computational methods for determining effective material properties. Those can then be used e.g. in a purely macroscopic or in a truly two-scale FE simulations [23, 24, 25]. Furthermore, multigrid coarsening strategies for upscaling were proposed in [26, 27, 28]. For merely statistically periodic cellular solids, fundamental cells are referred to as representative volume elements [29], representative elementary volumes [30] or statistical volume element [31], their size should be at least 5 inter-trabecular distances [32]. Their homogenization was already studied for instance in [33, 34].

Composite finite elements for geometrically complicated domains are a very effective approach to avoid nontrivial 3D tetrahedral meshing [35, 36, 37] of complicated domains as necessary for classical finite element methods. Instead of treating geometric complexity in geometrically complicated meshes with simple basis functions, so-called composite basis functions on regular structured meshes are used. Alternative approaches are the immersed interface methods [38, 39, 40], immersed finite elements [41, 42], generalized finite element methods [43, 44, 45], extended finite element methods [46], fictitious domain methods [47, 48, 49] and their combination with finite elements [50], weighted extended B-splines [51, 52], and unfitted meshes [53].

The composite finite element approach was first introduced in [54, 55, 56, 57] and presented for geometrically complicated domains on 3D regular hexahedral computational grids in [58]. Its application to homogenization for geometrically periodic microstructures was discussed in [59], and the homogenization for statistically periodic structures was proposed in [60] in the context of composite finite elements for discontinuous coefficients across geometrically complicated interfaces.

2 MATERIAL AND METHODS

In this section we will specify the concrete type of trabecular bone specimen investigated here. Then, tailored to this application scenario we develop the homogenization approach, empha-

sizing the interplay of the classical strain–stress based and a variational approach. Finally, we will derive the numerical algorithm based on a composite finite element discretization.

2.1 Trabecular Bone Specimens

Trabecular bone specimens were harvested from a young male (*human-y*) and an osteoporotic elderly female Caucasian human donor (*human-o*), and from a porcine and a bovine spine. Individual vertebral bodies were extracted, top and bottom end plates were removed using a band saw, leaving slices of 12 mm thickness. Cylindrical specimens were then extracted using a trepan of 8 mm diameter and bone marrow was removed using a water jet (Braun Oral-B Professional Care 6500, Kronberg, Germany). Six specimens for each individual were selected by visual inspection and assessment of structural damage by the sample extraction process and scanned in μ CT at 35 μ m (XCT FAN Beam μ -Scope, Stratec Medizintechnik GmbH, Pforzheim, Germany) and 8 bit resolution. The 3D dataset was resampled to 40 μ m resolution by trilinear interpolation, voxel values now being treated as floating point numbers. A segmentation threshold was determined based on the grey value histogram [61] and two cubes of 129^3 voxels (corresponding to 5.16 mm edge length) were extracted at the bottom and top of the cylindrical dataset. Thereby, the z axis in the datasets is the craniocaudal anatomical axis (up to orientation) whereas the dorsoventral and dextro-sinistral axes are no longer known and differ between specimens. Finally, subtracting the threshold from the voxel data yields an appropriate domain description where the zero level set describes the trabecular boundaries and negative values correspond to the interior. Two examples for each species are rendered in Fig. 1. For the trabecular structures, we assume a Young modulus $E = 13$ GPa and a Poisson ratio $\nu = 0.32$ which are realistic values for human trabecular bone [62]. Trabecular separation (Tb.Sp) was determined using a CT analysis software (CTAn, Skyscan, Kontich, Belgium) and local separation measurements of the porous structure. Volume based local separation is here defined via the identification of the largest sphere that includes the point of interest and that fits completely in the pore [63].

2.2 Numerical Homogenization

In this paragraph we first discuss a numerical homogenization technique for strictly periodic structures. Hence, we argue that the effective elasticity tensor satisfies all symmetry requirements expected from a physical point of view. The homogenization method is then adapted to the case of statistically representative fundamental cells so that it can be applied to trabecular bone specimens.

Let Ω denote the computational domain (for simplicity, we assume $\Omega = [0, 1]^3$) and $\Omega^\# \subset \Omega$ denote a fundamental lattice cell of the interior trabecular structure. The notation $\#$ is supposed to suggest both periodicity and trabecularity. Moreover, let

$$\begin{aligned} \partial^\# \Omega^\# &:= \partial \Omega^\# \cap \partial \Omega \\ \Omega_\beta^\# &:= \{x \in \Omega^\# \mid \text{dist}(x, \partial \Omega) > \beta\} \end{aligned} \tag{1}$$

so that $\partial^\# \Omega^\#$ is the ‘exterior boundary’ of the microstructure and $\Omega_\beta^\#$ is an interior part of the microstructure with (sufficient) distance β from the boundary of the computational domain to later avoid boundary artifacts.

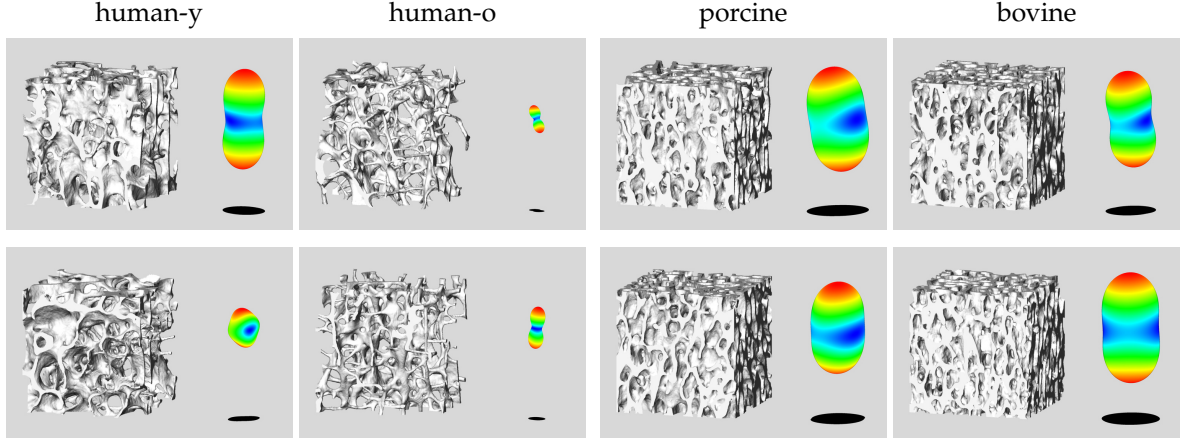


Figure 1: For each species, two specimens of trabecular bone are shown. The resulting effective elasticity tensors are visualized next to the specimens and from the same perspective (i. e. before optimizing axis alignment). The scale of the tensor visualization is the same for all human specimens (left two columns) and four times bigger than for all animal specimens (right two columns).

Moreover, C denote the microscopic linearized elasticity tensor for our trabecular structure and is given in the usual tensor notation as

$$C_{ijkl} = \lambda \delta_{ij} \delta_{kl} + \mu (\delta_{il} \delta_{jk} + \delta_{ik} \delta_{jl}) \quad (2)$$

where $\lambda = \frac{E\nu}{(1+\nu)(1-2\nu)} \approx 8.754$ GPa and $\mu = \frac{E}{2(1+\nu)} \approx 4.924$ GPa.

Numerical Homogenization for Periodic Structures. Let us first discuss the strain–stress type ‘cell problem’ approach (cf. [64, Chapter 1]) used in homogenization on strictly periodic fundamental cells $\Omega^\#$ and given microscopic elasticity tensor C . In this approach, a set of unit macroscopic strains \bar{u} is used to compute periodic correction profiles \tilde{u} (by a microscopic simulation) and to evaluate the actual physical equilibrium displacements $u = \bar{u} + \tilde{u}$. From this, a resulting average stress $\bar{\sigma}$ can be derived, yielding the entries of a macroscopic elasticity tensor \bar{C} . This approach involves solving the problem

$$-\operatorname{div}(C\epsilon(u)) = 0 \quad \Rightarrow \quad -\operatorname{div}(C\epsilon(\tilde{u})) = \operatorname{div}(C\epsilon(\bar{u})) \quad (3)$$

Given the material stiffness and a specimen weight of several 100 mg, volume forces (such as gravity) are ignored here. The variational formulation of (3) is given by

$$\int_{\Omega^\#} C\epsilon(\tilde{u}) : \epsilon(v) = - \int_{\Omega^\#} C\epsilon(\bar{u}) : \epsilon(v) \quad \forall v \in H_\#^{1,2}(\Omega^\#; \mathbb{R}^3) \quad (4)$$

for the displacement $\tilde{u} \in H_\#^{1,2}(\Omega^\#; \mathbb{R}^3)$ with the additional condition $\int_{\Omega^\#} \tilde{u} = 0$ to ensure uniqueness of the decomposition. Here, the function space $H_\#^{1,2}(\Omega^\#; \mathbb{R}^3)$ denotes the usual Sobolev space $H^{1,2}$ of vector-valued functions which fulfill periodic boundary conditions.

The effective elasticity tensor $\bar{C} = (\bar{C}_{ijkl})_{ijkl}$ couples macroscopic strain $\epsilon(\bar{u})$ and stress $\bar{\sigma}$ via $\bar{\sigma} = \bar{C}\epsilon(\bar{u})$, where the effective stress is evaluated as $\bar{\sigma} = \int_{\Omega^\#} C\epsilon(\bar{u} + \tilde{u})$. To determine \bar{C} one has to consider sufficiently many displacements \bar{u}^{ij} for $i, j \in \{0, 1, 2\}$ (due to symmetry of

stress and strain, 6 are actually sufficient) with linearly independent strain tensors. In explicit we choose $\epsilon(\bar{u}^{ij}) = e_{ij} := \frac{1}{2}(e_i \otimes e_j + e_j \otimes e_i)$. and obtain $\bar{C}_{..ij} = \bar{\sigma}^{ij} = \int_{\Omega^\#} C(\epsilon(\bar{u}^{ij}) + e_{ij})$, where \bar{u}^{ij} solves (4) for given \bar{u}^{ij} . Microscopic symmetry of stress and strain ensure the symmetries $\bar{C}_{ijkl} = \bar{C}_{jikl} = \bar{C}_{ijlk}$ also for the homogenized elasticity tensor. For physical reasons, the symmetry $\bar{C}_{ijkl} = \bar{C}_{klij}$ also needs to be satisfied. Practically, one observes a lack of the this symmetry in case of the resulting, numerically computed elasticity tensors. This effect vanishes in numerical experiments for decreasing grid size and smooth microscopic domain shape. Hence, it turns out to be mathematically more convenient to use another variational formulation with the same Euler–Lagrange equation (in the continuous case) instead: For given macroscopic displacement \bar{u} , find the minimizer \tilde{u} in

$$\int_{\Omega^\#} \bar{C}\epsilon(\bar{u}) : \epsilon(\bar{u}) = \inf_{\tilde{v} \in H_{\#}^{1,2}(\Omega; \mathbb{R}^3)} \int_{\Omega^\#} C\epsilon(\bar{u} + \tilde{v}) : \epsilon(\bar{u} + \tilde{v}). \quad (5)$$

In fact, the entries \bar{C}_{ijkl} of the symmetric tensor \bar{C} can be obtained from the already computed strains e_{ij} using the formula

$$C_{ijkl} = Ce_{ij} : e_{kl} = (Ce_{ij+kl} : e_{ij+kl} - Ce_{ij-kl} : e_{ij-kl}), \quad (6)$$

where $e_{ij\pm kl} := \frac{1}{2}(e_{ij} \pm e_{kl})$, and \bar{u}^{ij} with $\epsilon(\bar{u}^{ij}) = e_{ij}$. Indeed, we obtain

$$\begin{aligned} \bar{C}_{ijkl} &= \int_{\Omega^\#} \bar{C}\epsilon(\bar{u}^{ij}) : \epsilon(\bar{u}^{kl}) = \int_{\Omega^\#} \bar{C}\epsilon(\bar{u}^{ij+kl}) : \epsilon(\bar{u}^{ij+kl}) - \bar{C}\epsilon(\bar{u}^{ij-kl}) : \epsilon(\bar{u}^{ij-kl}) \\ &= \int_{\Omega^\#} C\epsilon(\bar{u}^{ij+kl} + \bar{u}^{ij+kl}) : \epsilon(\bar{u}^{ij+kl} + \bar{u}^{ij+kl}) - C\epsilon(\bar{u}^{ij-kl} + \bar{u}^{ij-kl}) : \epsilon(\bar{u}^{ij-kl} + \bar{u}^{ij-kl}) \end{aligned} \quad (7)$$

where $\epsilon(\bar{u}^{ij\pm kl}) = \frac{1}{2}(e_{ij} \pm e_{kl})$ and $\bar{u}^{ij\pm kl}$ is the corresponding solution of (4). By definition the resulting elasticity tensors \bar{C} are now symmetric.

An argument in favor of the variational approach. In what follows, we will analyze the above lack of symmetry in numerical strain–stress homogenization approach. Therefore, we will first demonstrate that under sufficient smoothness assumptions on the microscopic elasticity tensor C , the macroscopic tensor \bar{C} obtained either from (4) or from (5) coincide.

Using Einstein summation convention and the notation $w_{,i} = \partial_i w$ for partial derivatives, we first observe

$$-(C_{ijkl}\tilde{u}_{l,k}^{mn})_{,i} = (C_{ijmn})_{,i} \quad (8a)$$

$$\bar{\sigma}^{kl} = (\bar{C}_{ijmn}\epsilon(e_{kl})_{mn})_{ij} = (\bar{C}_{ijkl})_{ij} \quad (8b)$$

$$\bar{C}_{ijkl} = \bar{\sigma}_{ij}^{kl} = \int_{\Omega^\#} C_{ijkl}(\delta_{ik}\delta_{jl} + \tilde{u}_{j,i}^{kl}) \quad (8c)$$

where (8a) follows from (3) and the symmetry of C , (8b) follows from $\sigma = C\epsilon(u)$, $\epsilon(\bar{u}^{kl}) = e_{kl}$, and (8c) is the cell problem (4).

Then the desired symmetry holds due to

$$\begin{aligned}
\bar{C}_{ijkl} - \bar{C}_{klij} &\stackrel{(a)}{=} \int C_{ijmn} (\delta_{mk} \delta_{nl} + \tilde{u}_{n,m}^{kl}) - \int C_{klmn} (\delta_{mi} \delta_{nj} + \tilde{u}_{n,m}^{ij}) \\
&= \int C_{ijkl} - C_{klij} + C_{ijmn} \tilde{u}_{n,m}^{kl} - C_{klmn} \tilde{u}_{n,m}^{ij} \stackrel{(b)}{=} \int C_{ijmn} \tilde{u}_{n,m}^{kl} - C_{klmn} \tilde{u}_{n,m}^{ij} \\
&\stackrel{(c)}{=} \int -C_{ijmn,m} \tilde{u}_n^{kl} + C_{klmn,m} \tilde{u}_n^{ij} \stackrel{(d)}{=} \int -C_{mni,j} \tilde{u}_n^{kl} + C_{mnkl,m} \tilde{u}_n^{ij} \\
&\stackrel{(e)}{=} \int (C_{mnpq} \tilde{u}_{q,p}^{ij})_{,m} \tilde{u}_n^{kl} - (C_{mnpq} \tilde{u}_{q,p}^{kl})_{,m} \tilde{u}_n^{ij} \\
&\stackrel{(f)}{=} \int -C_{mnpq} \tilde{u}_{q,p}^{ij} \tilde{u}_{n,m}^{kl} + C_{mnpq} \tilde{u}_{q,p}^{kl} \tilde{u}_{n,m}^{ij} = 0
\end{aligned} \tag{9}$$

Here, the domain of integration $\Omega^\#$ is left out everywhere to keep notation simple. Step (a) is due to (8c), (b) uses the symmetry of the microscopic tensor, (c) results from an integration by parts with periodic boundary conditions, (d) again uses the symmetry of C , (e) takes into account Equation (8a), and (f) is again based on an integration by parts.

For $\epsilon(\tilde{u}^{ij\pm kl}) = e_{ij\pm kl}$, the periodic function $\tilde{u}^{ij\pm kl}$ solves

$$\int_{\Omega^\#} C\epsilon(\tilde{u}^{ij\pm kl}) : \epsilon(\theta) = - \int_{\Omega^\#} C\epsilon(\tilde{u}^{ij\pm kl}) : \epsilon(\theta) \tag{10}$$

for all test functions $\theta \in H_\#^{1,2}(\Omega^\#; \mathbb{R}^3)$, and $\tilde{u}^{ij\pm kl} = \frac{1}{2}(\tilde{u}^{ij} \pm \tilde{u}^{kl})$. Moreover,

$$\bar{\sigma}^{ij\pm kl} = \frac{1}{2}(\bar{\sigma}^{ij} \pm \bar{\sigma}^{kl}) = \int_{\Omega^\#} C\epsilon(\tilde{u}^{ij\pm kl} + \tilde{u}^{ij\pm kl}), \tag{11a}$$

$$0 = \int_{\Omega^\#} C\epsilon(\tilde{u}^{ij\pm kl} + \tilde{u}^{ij\pm kl}) : \epsilon(\theta) \tag{11b}$$

for all test functions $\theta \in H_\#^{1,2}(\Omega^\#; \mathbb{R}^3)$. Hence

$$\begin{aligned}
\bar{C}_{ijkl} &= \int \bar{C}_{ijkl} e_{ij} : e_{kl} \stackrel{(a)}{=} \int \bar{C}_{ijkl} \epsilon(\tilde{u}^{ij+kl}) : \epsilon(\tilde{u}^{ij+kl}) - \bar{C}_{ijkl} \epsilon(\tilde{u}^{ij-kl}) : \epsilon(\tilde{u}^{ij-kl}) \\
&\stackrel{(b)}{=} \int C_{ijkl} \epsilon(\tilde{u}^{ij+kl} + \tilde{u}^{ij+kl}) : \epsilon(\tilde{u}^{ij+kl} + \tilde{u}^{ij+kl}) - C_{ijkl} \epsilon(\tilde{u}^{ij-kl} + \tilde{u}^{ij-kl}) : \epsilon(\tilde{u}^{ij-kl} + \tilde{u}^{ij-kl}) \\
&\stackrel{(c)}{=} \int C_{ijkl} \epsilon(\tilde{u}^{ij+kl} + \tilde{u}^{ij+kl}) : \epsilon(\tilde{u}^{ij+kl}) - C_{ijkl} \epsilon(\tilde{u}^{ij-kl} + \tilde{u}^{ij-kl}) : \epsilon(\tilde{u}^{ij-kl}) \\
&\stackrel{(d)}{=} \frac{1}{4} \left[(\bar{\sigma}^{ij} + \bar{\sigma}^{kl}) : (e_{ij} + e_{kl}) - (\bar{\sigma}^{ij} - \bar{\sigma}^{kl}) : (e_{ij} - e_{kl}) \right] \\
&\stackrel{(e)}{=} \frac{1}{4} (\hat{C}_{ijij} + \hat{C}_{ijkl} + \hat{C}_{klij} + \hat{C}_{klkl}) - \frac{1}{4} (\hat{C}_{ijij} - \hat{C}_{ijkl} - \hat{C}_{klij} + \hat{C}_{klkl}) \\
&= \frac{1}{2} (\hat{C}_{ijkl} + \hat{C}_{klij})
\end{aligned} \tag{12}$$

where \hat{C} denotes the homogenized tensor obtained by the strain–stress cell problem formulation above. Here, step (a) uses the symmetry of \bar{C} in the first two and in the last two indices and (6), step (b) results from \tilde{u} solving the cell problem, step (c) uses that the \tilde{u} are admissible as test functions, step (d) takes into account (11a), step (e) refers to the property (8c) for

\hat{C} . Finally the symmetry of \hat{C} already proved above in (9) shows that the two tensors are equivalent, so the symmetry of \bar{C} holds.

The above argumentation requires the microscopic elastic stress $C\epsilon(\bar{u})$ to be differentiable on the domain $\Omega^\#$. This surely true in the continuous case but fails to hold in the spatially discrete case. Indeed, for a piecewise affine and continuous displacement, the resulting stress will jump on grid cell boundaries. We consider this as the reason for the numerically observed lack of symmetry. Hence, numerically it is advisable to consider the variational definition of the homogenized elasticity tensors at basically no additional computational cost.

Numerical Homogenization for Statistically Periodic Trabecular Structures. Let us now briefly sketch the numerical homogenization procedure for statistically periodic trabecular microstructures. For more details (in the case of discontinuous coefficients) we refer to [60]. In this case, there is no useful notion of periodic boundary conditions for the correction profile. Instead, a macroscopic strain $\epsilon(\bar{u})$ is prescribed by (Dirichlet) displacement boundary conditions on $\partial^\# \Omega^\#$. To compensate for boundary artifacts (artificial stiffening due to the Dirichlet boundary conditions), the evaluation of the average stress $\bar{\sigma}$ is restricted to the proper interior subset $\Omega_\beta^\#$ of the structure. Note that $\Omega_\beta^\#$ is the set that still needs to be statistically representative for the microstructure. As the simulation needs to be run on whole $\Omega^\#$, one needs to find a trade-off between sufficiently large boundary layer ($\beta > 0$) and sufficiently small computational overhead ($\beta \ll 0.5$). In our applications, the value $\beta = 0.125$ is chosen because it corresponds to approximately one inter-trabecular distance for the animal specimens and leads to sufficiently reliable results for the human species, cf. Table 2. Ün et al. [65] obtain the same thickness of a boundary layer to be ignored in a similar approach. They, however, use cylindrical specimens and model a standard mechanical experiment with stress-free side boundary, leading to artificial softening of the structure compared to its in situ properties.

For \bar{u}^{ij} , $i, j = 0, 1, 2$, defined as above, we solve the microscopic problems

$$\begin{aligned} -\operatorname{div}(C\epsilon(u^{ij})) &= 0 & \text{in } \Omega^\# \\ u^{ij} &= \bar{u}^{ij} & \text{on } \partial^\# \Omega^\# \end{aligned} \quad (13)$$

for u^{ij} . The average stress is then evaluated as

$$\bar{\sigma}^{ij} = \int_{\Omega_\beta^\#} C\epsilon[u^{ij}]. \quad (14)$$

Due to $\epsilon(u^{ij}) = \epsilon(u^{ji})$ and (6), it is in fact sufficient to perform six instead of nine simulations, automatically yielding a symmetric effective tensor \bar{C} .

Tensor Visualization. The macroscopic elasticity tensor \bar{C} can be visualized following the proposal in [66, 67] where the quantities $N = n \otimes n$ ($N_{ij} = n_i n_j$), $S = \bar{C}N$ ($S_{ij} = \bar{C}_{ijkl} N_{kl}$) and finally $\sigma = N : S$ ($\sigma = N_{ij} S_{ij}$) are computed and then the shape $\{\sigma \cdot n \mid \|n\| = 1\}$ is rendered as a representation of the compressive stiffness in different directions. Furthermore, the bulk modulus $\operatorname{tr} S = \sum_i S_{ii}$ is used to color the deformed sphere.

Tensor Rotation. Once we have computed the effective elasticity tensor $\bar{\mathbb{C}}$, orthotropy cannot be verified immediately because the orthotropy axes are not necessarily aligned with the coordinate axes. So we follow [68, 69] and determine a rotation matrix $Q = (Q_{ab})_{ab}$ such that the elasticity tensor $\bar{\mathbb{C}}$ rotated by Q minimizes a non-orthotropy defect

$$F_{\bar{\mathbb{C}}}(Q) = \frac{\|R_a[Q_{mi}Q_{nj}Q_{pk}Q_{ql}\bar{\mathbb{C}}_{ijkl}]\|_{\mathbb{F}}^2}{\|R_b[Q_{mi}Q_{nj}Q_{pk}Q_{ql}\bar{\mathbb{C}}_{ijkl}]\|_{\mathbb{F}}^2} \quad (15)$$

where R_a is the restriction to the entries not present in an aligned orthotropic tensor and R_b the one to those present (upper left block and diagonal of lower right block in Voigt's notation). The rotation Q is described by roll, pitch, and yaw angles, all in the range $[-45^\circ, 45^\circ]$ because we are only interested in the axes up to orientation. Indeed, one observe that $F_{\bar{\mathbb{C}}}(Q(\text{roll}, \text{pitch}, \text{yaw}))$ is a rather smooth function of the angles. Hence, the minimization is performed by evaluating $F_{\bar{\mathbb{C}}}$ at discrete angle triples and nesting intervals until a 'discrete' minimum is reached. The computational workload of this simple optimization strategy as a postprocessing step is negligible compared to the computational cost of the simulations required for the actual numerical homogenization.

2.3 Composite Finite Elements for Numerical Homogenization

For the discretization of the elasticity problems (13) above, we use composite finite elements. We will give a brief explanation of the method here and refer the reader to [58] for more details on the method and its implementation.

The basic idea of composite finite elements for geometrically complicated domains is that a regular hexahedral computational grid (divided in tetrahedra) is used together with piecewise affine-linear basis functions multiplied by the characteristic function of a discretization $\Omega^{\# \boxtimes}$ of the microstructure $\Omega^\#$.

Let ϕ be the level set function describing $\Omega^\# = \{\phi < 0\}$, obtained from voxel image data corresponding to a regular hexahedral grid \mathcal{G}^\square . Moreover, let ϕ^{\boxtimes} be its piecewise affine-linear approximation on the regular tetrahedral grid \mathcal{G}^{\boxtimes} obtained from the regular hexahedral grid. Note that a piecewise multilinear approximation would be the natural choice for voxel data, but ϕ^{\boxtimes} differs from this only by a negligible amount compared to noise of the image acquisition process. $\Omega^{\# \boxtimes} = \{\phi^{\boxtimes} < 0\}$ is then an approximation of the trabecular microstructure with piecewise planar boundary.

For ψ_i^{\boxtimes} being standard piecewise affine (scalar) finite element basis functions on \mathcal{G}^{\boxtimes} indexed over all nodes, composite finite element basis functions ψ_i^{CFE} are defined as

$$\psi_i^{\text{CFE}} := \psi_i^{\boxtimes} \chi_{\Omega^{\# \boxtimes}}. \quad (16)$$

This means that basis functions whose support lies completely within $\Omega^{\# \boxtimes}$ are not modified at all, those ψ_i^{\boxtimes} whose support is intersected by the interior boundary of $\Omega^{\# \boxtimes}$ are cut off and restricted to the trabecular microstructure, and those basis functions with support lying completely outside $\Omega^{\# \boxtimes}$ are set to zero and are ignored further on. Let us remark that all regular hexahedral grid nodes inside $\Omega^{\# \boxtimes}$ and one layer of nodes outside are assigned degrees of freedom. In the vector-valued elasticity problem we consider here, the spatial components of the displacement are discretized separately, resulting in 3 degrees of freedom per grid node.

For the assembly of the finite element matrices in an element-by-element way, a virtual subdivision of the polyhedra $T \cap \Omega^{\# \boxtimes}$ for tetrahedra T of \mathcal{G}^{\boxtimes} is performed so that a ‘virtual’ tetrahedral grid \mathcal{G}^{Δ} is obtained (but never stored explicitly). The basis functions ψ_i^{CFE} can now be interpreted as composed of standard piecewise affine-linear ‘virtual’ basis functions on \mathcal{G}^{Δ} by linear combination—hence the term ‘composite’.

The uniform hexahedral structure of \mathcal{G}^{\boxtimes} enables the use of geometric multigrid solvers for the resulting systems of linear equations. Such a multigrid solver, which includes an appropriate treatment of the Dirichlet boundary, is explained in [58].

Let us remark that there is no bound on the aspect ratio of the virtual tetrahedra (other than the restriction that ψ must not be zero at regular grid points). This would lead to poor condition numbers of the finite element matrices [70] in a single grid solver. The gradients of the basis functions ψ_i^{CFE} , however, does not degenerate because they are merely the gradients of standard basis functions ϕ^{\boxtimes} on the regular tetrahedral grid. The multigrid method encounters difficulties if (geometrically) coarsened basis functions have disconnected support with components in physically weakly coupled parts of the trabecular structure. In this case, inappropriate coarse grid corrections in the multigrid solver can lead to poor convergence rates. This effect can be remedied by choosing a sufficiently fine level in the hierarchy of coarsened grids as coarsest level in the multigrid method (where an explicit solver is applied).

3 RESULTS

The average trabecular spacings for the different species are listed in Table 1, showing that the animal specimens are substantially larger (with smaller trabecular spacing) than the human specimens. The width β of the boundary layer ignored for evaluating stresses is addressed in Table 2 where macroscopic elasticity tensors were determined for different widths of the boundary layer and the corresponding compressive stiffnesses were computed. Due to the smaller trabecular spacing, the animal specimens permit smaller values for β than the human specimens. Nevertheless, for better comparison we chose the value $\beta = 0.125$ for all specimens.

Table 3 lists entry-wise averaged macroscopic elasticity tensors for each species in Voigt’s notation in detail. The left plot in Fig. 2 compares the compressive stiffnesses in the two non-cranio-caudal directions x and y . Information about the dorsoventral and dextro-sinistral axis is not available. Thus, we proceed with the computation of an averaged transverse compressive stiffness. These values are listed in Table 1.

The cranio-caudal compressive stiffness (direction z) is plotted against average compressive stiffness in a scatter plot in the right plot in Fig. 2 and an average anisotropy for the different species is listed in Table 1 (concerning these numbers, note that averaging and division do not commute). Comparing the anisotropies, we observe that in pigs, cranio-caudal stiffness is only about 1.9 times the transverse one whereas the ratio in cows is about 2.6. These ratios are approximately 2.4 for our non-osteoporotic human specimens and 2.9 for the osteoporotic ones. For the human osteoporotic specimens, we observe 53 % smaller cranio-caudal compressive stiffness compared to the non-osteoporotic specimens whereas transverse stiffness decreases by 61 %. Table 1 also lists shearing stiffnesses G_{xy} in the transverse x, y plane and the mean

Table 1: For the different species considered, the table lists the average trabecular spacing Tb.Sp in mm and their standard deviations as well as the edge length of the evaluation domain $\Omega_{\beta=0.125}^{\#}$ (defined in Equation (1)) in units of Tb.Sp. Volume fraction is the amount of trabecular volume relative to the bounding box. Average compressive stiffnesses in craniocaudal (E_{zz}) and transverse direction ($(E_{xx} + E_{yy})/2$) and the shear stiffnesses in the transverse plane (G_{xy}) and the mean of the shear stiffnesses in the sagittal and coronal plane ($(G_{yz} + G_{zx})/2$) are listed along with the respective standard deviations. Moreover, the anisotropy ratio $2E_{zz}/(E_{xx} + E_{yy})$ between craniocaudal and average transverse compressive stiffness is computed.

species	human-y	human-o	porcine	bovine
Tb.Sp in mm	0.918 ± 0.128	1.060 ± 0.113	0.426 ± 0.011	0.490 ± 0.071
edge length of $\Omega_{\beta=0.125}^{\#}$ in Tb.Sp	4.22	3.65	9.08	7.90
volume fraction	0.141 ± 0.017	0.081 ± 0.022	0.370 ± 0.016	0.330 ± 0.033
E_{zz} in GPa	0.812 ± 0.246	0.383 ± 0.130	3.456 ± 0.295	3.203 ± 0.433
$(E_{xx} + E_{yy})/2$ in GPa	0.334 ± 0.130	0.130 ± 0.099	1.831 ± 0.173	1.263 ± 0.331
$2E_{zz}/(E_{xx} + E_{yy})$	2.550 ± 0.838	4.054 ± 1.825	1.891 ± 0.109	2.635 ± 0.474
G_{xy} in GPa	0.110 ± 0.043	0.042 ± 0.032	0.705 ± 0.075	0.475 ± 0.117
$(G_{yz} + G_{zx})/2$ in GPa	0.182 ± 0.042	0.068 ± 0.049	0.939 ± 0.084	0.739 ± 0.135

shearing stiffnesses averaged for the sagittal and coronal plane, being larger than G_{xy} for all species.

Finally, Fig. 3 shows two more porcine specimens that were obtained from the same bovine vertebra. They are part of the same cylindrical dataset and thus have a distance of about 2 mm in craniocaudal direction. Moreover, the orientations in x and y direction are the same for both specimens. The resulting tensors and rotation angles, however, differ significantly, compressive stiffness in z direction by 33 % and the yaw angle by 44 %. This indicates that the trabecular interior of a whole vertebral body cannot be viewed as an effectively homogeneous material with spatially constant properties.

For the simulations for the leftmost (human-y) specimen in Fig. 1 at resolution 129^3 , the Composite FE discretization resulted in a 3×3 block matrix using 1158.6 MiB of memory, where the solver took 6755.6 seconds of cpu time on an Opteron 3 GHz processor on average for each of the six different settings of boundary conditions and a reduction of the residuum by eight orders of magnitude. For the (more dense) rightmost (bovine) specimen, matrix memory consumption was 1808.8 MiB and solver cpu time was 14 426.5 seconds.

4 CONCLUSION

This paper is an application study of numerical homogenization methodology in the area of biomechanics of trabecular bone. In particular it underlines that a reliable extraction of homogenized mechanical properties is feasible and can be used in future truly two scale simulation tools. Let us briefly discuss some aspects of the presented approach and draw conclusions.

The listings of averaged tensors in Table 3 exhibit a small orthotropy defect after finding the axes of orthotropy. The slightly bigger orthotropy defect for the osteoporotic human specimens compared to the non-osteoporotic and animal ones may indicate actual material properties or may be due to specimens being too small.

Table 2: For one specimen of each species (those in the top row of Fig. 1), macroscopic elasticity tensors are determined using evaluation domains excluding different boundary layers of width β . The table lists the resulting compressive stiffnesses in direction of the optimal orthotropy axes in units of GPa.

β	human-y			human-o			porcine			bovine		
	E_{xx}	E_{yy}	E_{zz}									
0/16	0.389	0.368	1.024	0.107	0.151	0.300	1.812	2.101	3.628	1.392	1.858	3.519
1/16	0.255	0.298	0.975	0.064	0.105	0.283	1.656	1.959	3.568	1.218	1.735	3.438
2/16	0.293	0.231	0.914	0.053	0.092	0.254	1.613	2.012	3.635	1.232	1.735	3.426
3/16	0.258	0.197	0.886	0.052	0.083	0.232	1.585	2.012	3.620	1.238	1.741	3.364
4/16	0.309	0.194	0.953	0.043	0.086	0.231	1.663	2.005	3.747	1.238	1.741	3.364

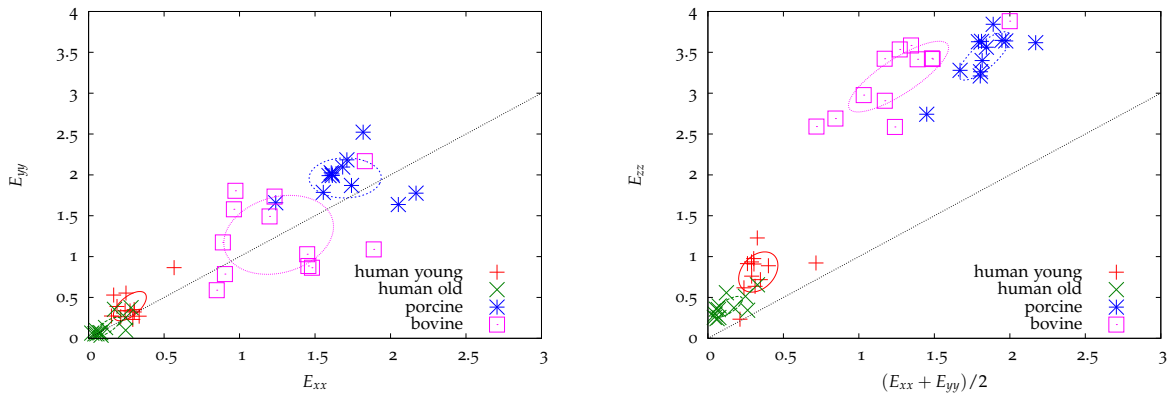


Figure 2: The *left* plot shows a scatter plot of the compressive stiffnesses in the transverse directions for the different species. On the *right*, the compressive stiffness in craniocaudal direction is plotted against the average transverse compressive stiffness. The ellipses in both cases show one standard deviation resulting from a principle component analysis for each species.

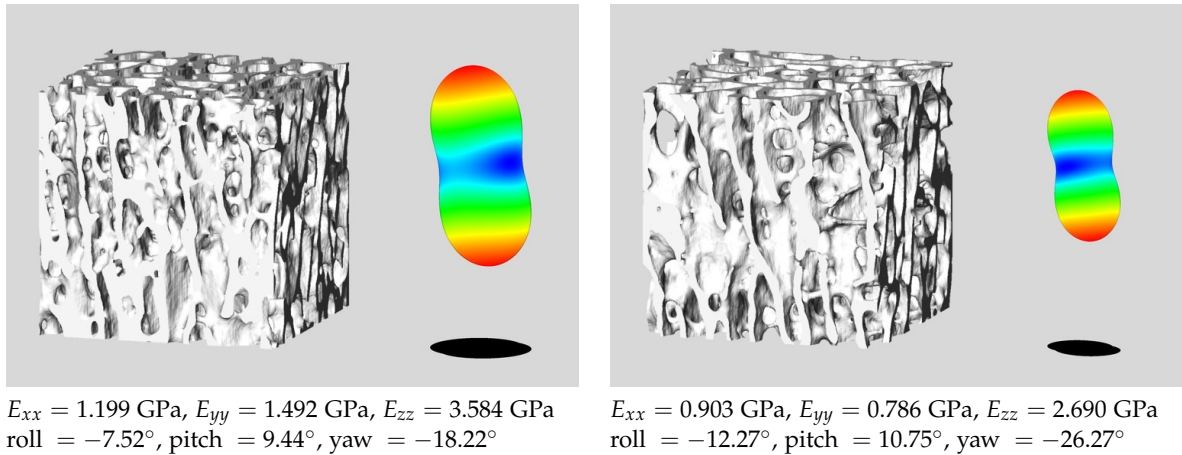


Figure 3: Two specimens from the same bovine vertebral body, spaced apart approximately 2 mm in craniocaudal direction and with the same x and y orientation, are visualized with their homogenized tensors in the same way as in Fig. 1.

Table 3: For each species, the elasticity tensor in Voigt's notation are averaged in each entry along with standard deviations. Entries for which the absolute value of the average plus the standard deviation is smaller than 0.02 times the maximal entry are listed in grey.

$$\begin{aligned}
\bar{\mathbf{C}}_{\text{hu-y}} &= \begin{pmatrix} 0.357 \pm 0.125 & 0.176 \pm 0.049 & 0.176 \pm 0.037 & -0.002 \pm 0.009 & -0.003 \pm 0.016 & 0.005 \pm 0.010 \\ 0.176 \pm 0.049 & 0.502 \pm 0.196 & 0.202 \pm 0.040 & 0.001 \pm 0.011 & -0.004 \pm 0.008 & 0.001 \pm 0.008 \\ 0.176 \pm 0.037 & 0.202 \pm 0.040 & 0.940 \pm 0.258 & -0.002 \pm 0.008 & 0.003 \pm 0.007 & -0.001 \pm 0.011 \\ -0.002 \pm 0.009 & 0.001 \pm 0.011 & -0.002 \pm 0.008 & 0.208 \pm 0.059 & -0.003 \pm 0.007 & -0.006 \pm 0.006 \\ -0.003 \pm 0.016 & -0.004 \pm 0.008 & 0.003 \pm 0.007 & -0.003 \pm 0.007 & 0.159 \pm 0.034 & -0.001 \pm 0.008 \\ 0.005 \pm 0.010 & 0.001 \pm 0.008 & -0.001 \pm 0.011 & -0.006 \pm 0.006 & -0.001 \pm 0.008 & 0.112 \pm 0.044 \end{pmatrix} \\
\bar{\mathbf{C}}_{\text{hu-o}} &= \begin{pmatrix} 0.150 \pm 0.105 & 0.057 \pm 0.039 & 0.065 \pm 0.043 & -0.003 \pm 0.008 & 0.004 \pm 0.008 & 0.002 \pm 0.008 \\ 0.057 \pm 0.039 & 0.173 \pm 0.141 & 0.080 \pm 0.059 & -0.001 \pm 0.009 & 0.002 \pm 0.005 & -0.001 \pm 0.004 \\ 0.065 \pm 0.043 & 0.080 \pm 0.059 & 0.439 \pm 0.155 & 0.000 \pm 0.003 & -0.001 \pm 0.004 & -0.001 \pm 0.003 \\ -0.003 \pm 0.008 & -0.001 \pm 0.009 & 0.000 \pm 0.003 & 0.080 \pm 0.057 & -0.001 \pm 0.003 & 0.001 \pm 0.003 \\ 0.004 \pm 0.008 & 0.002 \pm 0.005 & -0.001 \pm 0.004 & -0.001 \pm 0.003 & 0.059 \pm 0.041 & -0.001 \pm 0.002 \\ 0.002 \pm 0.008 & -0.001 \pm 0.004 & -0.001 \pm 0.003 & 0.001 \pm 0.003 & -0.001 \pm 0.002 & 0.043 \pm 0.033 \end{pmatrix} \\
\bar{\mathbf{C}}_{\text{po}} &= \begin{pmatrix} 1.581 \pm 0.429 & 0.626 \pm 0.136 & 0.740 \pm 0.142 & 0.001 \pm 0.013 & 0.005 \pm 0.018 & -0.015 \pm 0.018 \\ 0.626 \pm 0.136 & 1.585 \pm 0.583 & 0.729 \pm 0.171 & -0.004 \pm 0.016 & 0.005 \pm 0.013 & 0.013 \pm 0.018 \\ 0.740 \pm 0.142 & 0.729 \pm 0.171 & 3.700 \pm 0.496 & 0.001 \pm 0.008 & -0.002 \pm 0.009 & 0.006 \pm 0.022 \\ 0.001 \pm 0.013 & -0.004 \pm 0.016 & 0.001 \pm 0.008 & 0.735 \pm 0.187 & 0.002 \pm 0.018 & 0.001 \pm 0.008 \\ 0.005 \pm 0.018 & 0.005 \pm 0.013 & -0.002 \pm 0.009 & 0.002 \pm 0.018 & 0.745 \pm 0.138 & 0.002 \pm 0.011 \\ -0.015 \pm 0.018 & 0.013 \pm 0.018 & 0.006 \pm 0.022 & 0.001 \pm 0.008 & 0.002 \pm 0.011 & 0.477 \pm 0.116 \end{pmatrix} \\
\bar{\mathbf{C}}_{\text{bo}} &= \begin{pmatrix} 2.119 \pm 0.294 & 0.895 \pm 0.079 & 0.942 \pm 0.096 & -0.006 \pm 0.013 & -0.001 \pm 0.013 & 0.009 \pm 0.013 \\ 0.895 \pm 0.079 & 2.453 \pm 0.303 & 1.022 \pm 0.104 & -0.007 \pm 0.027 & 0.000 \pm 0.014 & -0.001 \pm 0.021 \\ 0.942 \pm 0.096 & 1.022 \pm 0.104 & 4.064 \pm 0.350 & 0.005 \pm 0.016 & 0.003 \pm 0.009 & 0.003 \pm 0.009 \\ -0.006 \pm 0.013 & -0.007 \pm 0.027 & 0.005 \pm 0.016 & 0.982 \pm 0.104 & -0.005 \pm 0.008 & -0.007 \pm 0.009 \\ -0.001 \pm 0.013 & 0.000 \pm 0.014 & 0.003 \pm 0.009 & -0.005 \pm 0.008 & 0.897 \pm 0.093 & -0.002 \pm 0.008 \\ 0.009 \pm 0.013 & -0.001 \pm 0.021 & 0.003 \pm 0.009 & -0.007 \pm 0.009 & -0.002 \pm 0.008 & 0.706 \pm 0.075 \end{pmatrix}
\end{aligned}$$

The results in Fig. 3 indicate that a numerical model for a full vertebral body should be a full two-scale model. The trabecular structure resolved at the microscale should be homogenized numerically (as presented in this paper) to obtain effective material properties at a mesoscale. This mesoscale, not resolving individual trabeculae, should account for spatial variations in the trabecular interior of the vertebral body, and should also include geometry and local properties of the cortical shell. For the second homogenization step to the macroscale (whole vertebral body) with spatially varying and possibly discontinuous material properties, Composite Finite Elements for discontinuous coefficients [60], among many other methods, can be used.

Given the CT scan datasets (thus ignoring the specimen acquisition and scanning process), only little user interaction is required to perform the numerical homogenization using Composite FE simulations. In particular, no meshing step (as in classical FE approaches) is necessary.

An experimental validation of the composite finite element method including the segmentation is still work in progress. A better theoretical understanding of the non-periodic homogenization method could also help with the appropriate choice of the boundary parameter β . Furthermore, an assumption of similar microscopic material properties for human, bovine and porcine specimens was quite questionable. It could be assumed that the constituents of bone tissue, collagen type I and hydroxyapatite, are the same across mammals [71]. However, the submicroscopic setup could be different resulting in different microscopic material properties. This fact remains unclear and needs further investigation.

Acknowledgments The authors thank Hendrik Hug for determining the geometric properties (such as trabecular spacings) of the specimens and the Hausdorff Center for Mathematics for providing computational resources. Ole Schwen was supported by the DFG project ‘Multiscale Simulation and Validation of the Elastic Microstructures of Vertebral Bodies’.

References

- [1] Tony M. Keaveny, Elise F. Morgan, Glen L. Niebur, and Oscar C. Yeh. Biomechanics of trabecular bone. *Annual Review of Biomedical Engineering*, 3:307–333, 2001.
- [2] A. Randell, P. N. Sambrook, T. V. Nguyen, H. Lapsley, G. Jones, P. J. Kelly, and J. A. Eisman. Direct clinical and welfare costs of osteoporotic fractures in elderly men and women. *Osteoporosis International*, 5:427–432, 1995.
- [3] Robert Marcus. The nature of osteoporosis. *Journal of Clinical Endocrinology and Metabolism*, 81:1–5, 1996.
- [4] Elizabeth R. Myers and Sara E. Wilson. Biomechanics of osteoporosis and vertebral fracture. *Spine*, 22(24):25S–31S, 1997.
- [5] European Foundation for Osteoporosis and National Osteoporosis Foundation of the USA. Consensus development statement – who are candidates for prevention and treatment for osteoporosis? *Osteoporosis International*, 7:1–6, 1997.
- [6] J. A. Kanis and O. Johnell. Requirements for DXA for the management of osteoporosis in Europe. *Osteoporosis International*, 16:229–238, 2005.
- [7] M. Richter, H.-J. Wilke, P. Kluger, L. Claes, and W. Puhl. Biomechanical evaluation of a newly developed monocortical expansion screw for use in anterior internal fixation of the cervical spine: In vitro comparison with two established internal fixation systems. *Spine*, 24(3):207–212, 1999.
- [8] Annette Kettler, Hans-Joachim Wilke, Rupert Dietl, Matthias Krammer, Christiano Lumenta, and Lutz Claes. Stabilizing effect of posterior lumbar interbody fusion cages before and after cyclic loading. *Neurosurgical Focus*, 92:87–92, 2000.
- [9] H.-J. Wilke, A. Kettler, and L. Claes. Primary stabilizing effect of interbody fusion devices for the cervical spine: an in vitro comparison between three different cage types and bone cement. *European Spine Journal*, 9:410–416, 2000.
- [10] M. J. Gardner, D. Demetrakopoulos, M. K. Shindle, M. H. Griffith, and J. M. Lane. Osteoporosis and skeletal fractures. *HSS Journal*, 2(1):62–69, 2006.
- [11] J. H. Chi and Z. L. Gokaslan. Vertebroplasty and kyphoplasty for spinal metastases. *Current Opinion in Supportive and Palliative Care*, 2(1):9–13, 2008.
- [12] E. Michael Lewiecki. Vertebroplasty and kyphoplasty update. *Current Osteoporosis Reports*, 6(3):114–119, 2008.
- [13] P. Fransen. Increasing pedicle screw anchoring in the osteoporotic spine by cement injection through the implant. Technical note and report of three cases. *Journal of Neurosurgery: Spine*, 7(3):366–369, 2007.
- [14] M. C. Chang, C. L. Liu, and T. H. Chen. Polymethylmethacrylate augmentation of pedicle screw for osteoporotic spinal surgery: a novel technique. *Spine*, 33(10):E317–E324, 2008.
- [15] Anne Polikeit, Stephen J. Ferguson, Lutz P. Nolte, and Tracy E. Orr. The importance of the endplate for interbody cages in the lumbar spine. *European Spine Journal*, 12:556–561, 2003.

- [16] S.-I. Chen, R.-M. Lin, and C.-H. Chang. Biomechanical investigation of pedicle screw – vertebrae complex: a finite element approach using bonded and contact interface conditions. *Medical Engineering & Physics*, 25:275–282, 2003.
- [17] Chen-Sheng Chen, Wen-Jer Chen, Cheng-Kung Cheng, Shya-Hua Eric Jao, Shan-Chang Chueh, and Chang-Chih Wang. Failure analysis of broken pedicle screws on spinal instrumentation. *Medical Engineering & Physics*, 25(6):487–496, July 2005.
- [18] B. van Rietbergen, R. Müller, D. Ulrich, P. Rügsegger, and R. Huiskes. Tissue stresses and strain in trabeculae of canine proximal femur can be quantified from computer reconstructions. *Journal of Biomechanics*, 32:165–173, 1999.
- [19] Liliana Rincón-Kohli and Philippe K. Zysset. Multi-axial mechanical properties of human trabecular bone. *Journal of Biomechanics and Modelling in Mechanobiology*, 8(3):195–208, 2009.
- [20] Yan Chevalier, Dieter Pahr, Helga Allmer, Mathieu Charlebois, and Philippe Zysset. Validation of a voxel-based FE method for prediction of the uniaxial apparent modulus of human trabecular bone using macroscopic mechanical tests and nanoindentation. *Journal of Biomechanics*, 40:3333–3340, 2007.
- [21] Luc Tartar. *Optimal Shape Design*, volume 1740 of *Lecture Notes in Mathematics*, chapter An Introduction to the Homogenization Method in Optimal Design, pages 47–156. Springer, 2001.
- [22] Todd Arbogast. *Current Trends in Scientific Computing*, chapter An overview of subgrid upscaling for elliptic problems in mixed form, pages 21–32. Contemporary Mathematics. AMS, 2003.
- [23] Thomas Y. Hou and Xiao-Hui Wu. A multiscale finite element method for elliptic problems in composite materials and porous media. *Journal of Computational Physics*, 134:169–189, 1997.
- [24] Todd Arbogast. *Numerical Treatment of Multiphase Flows in Porous Media*, volume 552 of *Lecture Notes in Physics*, chapter Numerical Subgrid Upscaling of Two-Phase Flow in Porous Media, pages 35–49. Springer, 2000.
- [25] Ana-Maria Matache and Christoph Schwab. Two-scale FEM for homogenization problems. *Mathematical Modelling and Numerical Analysis*, 36(4):537–572, 2002.
- [26] J. David Moulton, Joel E. Dendy Jr., and James M. Hyman. The black box multigrid numerical homogenization algorithm. *Journal of Computational Physics*, 142:80–108, 1998. Article No. CP985911.
- [27] Todd Arbogast, Susan E. Minkoff, and Philip T. Keenan. *Computational Methods in Contamination and Remediation of Water Resources*, volume 1 of *Computational Methods in Water Resources*, chapter An operator-based approach to upscaling the pressure equation, pages 405–412. Computational Mechanics Publications, 1998.
- [28] Achi E. Brandt. Methods of systematic upscaling. Technical Report MCS06-05, Weizmann Institute of Science, 2006.
- [29] S. J. Hollister and N. Kikuchi. A comparison of homogenization and standard mechanics analyses for periodic porous composites. *Computational Mechanics*, 10:73–95, 1992.
- [30] Y. Guéguen, M. Le Ravalec, and L. Ricard. Upscaling: Effective medium theory, numerical methods and the fractal dream. *Pure and Applied Geophysics*, 163:1175–1192, 2006.
- [31] Martin Ostoja-Starzewski. Material spatial randomness: From statistical to representative volume element. *Probabilistic Engineering Mechanics*, 21:112–132, 2006.
- [32] Timothy P. Harrigan, Murali Jasty, Robert W. Mann, and William H. Harris. Limitations of the continuum assumption in cancellous bone. *Journal of Biomechanics*, 21(4):269–275, 1988.

- [33] S. J. Hollister, D. P. Fyhrie, K. J. Jepsen, and S. A. Goldstein. Application of homogenization theory to the study of trabecular bone mechanics. *Journal of Biomechanics*, 24(9):825–839, 1991.
- [34] Lorna J. Gibson. Biomechanics of cellular solids. *Journal of Biomechanics*, 38:377–399, 2005.
- [35] Marshall Bern and David Eppstein. *Computing in Euclidian Geometry*, volume 1 of *Lecture Notes Series on Computing*, chapter Mesh generation and optimal triangulation, pages 23–90. World Scientific, Singapore, 1992.
- [36] Shang-Hua Teng and Chi Wai Wong. Unstructured mesh generation: Theory, practice and applications. *International Journal of Computational Geometry & Applications*, 10(3):227–266, 2000.
- [37] Jonathan Richard Shewchuk. What is a good linear element? Interpolation, conditioning, and quality measures. In *Proceedings of the 11th International Meshing Roundtable*, pages 115–126. Sandia National Laboratories, September 2002.
- [38] R. P. Beyer and R. J. LeVeque. Analysis of a one-dimensional model for the immersed boundary method. *SIAM Journal on Numerical Analysis*, 29(2):332–364, 1992.
- [39] Randall J. LeVeque and Zhi Lin Li. The immersed interface method for elliptic equations with discontinuous coefficients and singular sources. *SIAM Journal on Numerical Analysis*, 31(4):1019–1044, 1994.
- [40] Zhilin Li. A note on immersed interface method for three-dimensional elliptic equations. *Computers and Mathematics with Applications*, 31(3):9–17, February 1996.
- [41] Zhilin Li. The immersed interface method using a finite element formulation. *Applied Numerical Mathematics*, 27:253–267, 1998.
- [42] Zhilin Li, Tao Lin, and Xiaohui Wu. New Cartesian grid methods for interface problems using the finite element formulation. *Numerische Mathematik*, 1996(1):61–98, November 2003.
- [43] Jens Markus Melenk. *On Generalized Finite Element Methods*. Dissertation, University of Maryland, 1995.
- [44] C. A. Duarte, I. Babuška, and J. T. Oden. Generalized finite element methods for three-dimensional structural mechanics problems. *Computers & Structures*, 77:215–232, 2000.
- [45] Ivo Babuška, Uday Banerjee, and John E. Osborn. Survey of meshless and generalized finite element methods: A unified approach. *Acta Numerica*, 12:1–125, 2003.
- [46] T. Belytschko, N. Moës, S. Usui, and C. Parimi. Arbitrary discontinuities in finite elements. *International Journal for Numerical Methods in Engineering*, 50(4):993–1013, 2001.
- [47] G. P. Astrakhansev. Method of fictitious domain for a second-order elliptic equation with natural boundary conditions. *USSR Computational Mathematics and Mathematical Physics*, 18(1):114–121, 1978.
- [48] R. Glowinski and Yu. Kuznetsov. Distributed Lagrange multipliers based on fictitious domain method for second order elliptic problems. *Computer Methods in Applied Mechanics and Engineering*, 196:1498–1506, 2007.
- [49] Isabelle Ramière, Philippe Angot, and Michel Belliard. A fictitious domain approach with spread interface for elliptic problems with general boundary conditions. *Computer Methods in Applied Mechanics and Engineering*, 196:766–781, 2007.
- [50] A. Düster, J. Parvizian, Z. Yang, and E. Bank. The finite cell method for three-dimensional problems of solid mechanics. *Computer methods in applied mechanics and engineering*, 197(45–48):3768–3782, August 2008.

- [51] Klaus Höllig, Ulrich Reif, and Joachim Wipper. Weighted extended B-spline approximation of Dirichlet problems. *SIAM Journal on Numerical Analysis*, 39(2):442–462, 2001.
- [52] Klaus Höllig, Christian Apprich, and Anja Streit. Introduction to the Web-method and its applications. *Advances in Computational Mathematics*, 23:215–237, 2005.
- [53] John W. Barrett and Charles M. Elliott. A practical finite element approximation of a semi-definite Neumann problem on a curved domain. *Numerische Mathematik*, 51:23–36, 1987.
- [54] W. Hackbusch and S. A. Sauter. Composite finite elements for the approximation of PDEs on domains with complicated micro-structures. *Numerische Mathematik*, 75(4):447–472, 1997.
- [55] W. Hackbusch and S. A. Sauter. Composite finite elements for problems containing small geometric details. Part II: Implementation and numerical results. *Computing and Visualization in Science*, 1(1):15–25, 1997.
- [56] W. Hackbusch and S. Sauter. A new finite element approach for problems containing small geometric details. *Archivum Mathematicum*, 34:105–117, 1998. Equadiff 9 issue.
- [57] M. Rech, S. Sauter, and A. Smolianski. Two-scale composite finite element method for Dirichlet problems on complicated domains. *Numerische Mathematik*, 102:681–708, 2006.
- [58] Florian Liehr, Tobias Preusser, Martin Rumpf, Stefan Sauter, and Lars Ole Schwen. Composite finite elements for 3D image based computing. *Computing and Visualization in Science*, 12(4):171–188, April 2009.
- [59] Lars Ole Schwen, Uwe Wolfram, Hans-Joachim Wilke, and Martin Rumpf. Determining effective elasticity parameters of microstructured materials. In *Proceedings of the 15th Workshop on the Finite Element Method in Biomedical Engineering, Biomechanics and Related Fields*, pages 41–62. University of Ulm, July 2008.
- [60] Tobias Preusser, Martin Rumpf, Stefan Sauter, and Lars Ole Schwen. 3D composite finite elements for elliptic boundary value problems with discontinuous coefficients. 2010. submitted to SIAM Journal on Scientific Computing.
- [61] T. W. Ridler and S. Calvard. Picture thresholding using an iterative selection method. *IEEE Transactions on Systems, Man, and Cybernetics*, SMC-8(8):630–632, August 1978.
- [62] Uwe Wolfram, Hans-Joachim Wilke, and Philippe K. Zysset. Rehydration of vertebral trabecular bone: Influences on its anisotropy, its stiffness and the indentation work with a view to age, gender and vertebral level. *Bone*, 46:348–354, 2010.
- [63] T. Hildebrand and P. Rüegsegger. A new method for the model-independent assessment of thickness in three-dimensional images. *Journal of Microscopy*, 185(1):67–75, 1997.
- [64] Grégoire Allaire. *Shape optimization by the homogenization method*, volume 146 of *Applied Mathematical Sciences*. Springer-Verlag, New York, 2002.
- [65] Kerem Ün, Grant Bevil, and Tony M. Keaveny. The effects of side-artifacts on the elastic modulus of trabecular bone. *Journal of Biomechanics*, 39:1955–1963, 2006.
- [66] Q.-C. He and A. Curnier. A more fundamental approach to damaged elastic stress-strain relations. *International Journal for Solids and Structures*, 32(10):1433–1457, 1995.
- [67] Antonio Cazzani and Marco Rovati. Extrema of Young’s modulus for cubic and transversely isotropic solids. *International Journal of Solids and Structures*, 40:1713–1744, 2003.
- [68] B. Van Rietbergen, A. Odgaard, J. Kabel, and R. Huijkes. Direct mechanics assessment of elastic symmetries and properties of trabecular bone architecture. *Journal of Biomechanics*, 29(12):1653–1657, 1996. Technical Note.

- [69] P. K. Zysset, R. W. Goulet, and S. J. Hollister. A global relationship between trabecular bone morphology and homogenized elastic properties. *Journal of Biomedical Engineering*, 120:640–646, 1999.
- [70] Tobias Preusser, Martin Rumpf, and Lars Ole Schwen. Finite element simulation of bone microstructures. In *Proceedings of the 14th Workshop on the Finite Element Method in Biomedical Engineering, Biomechanics and Related Fields*, pages 52–66. University of Ulm, July 2007.
- [71] Anthony L. Mescher. *Junqueira's Basic Histology: Text and Atlas*. McGraw-Hill, 12th edition, 2009.